Published in the *Journal of Fluid Mechanics*, Vol. 782, pp. 37-62 (2015).

Vorticity Reconnection during Vortex Cutting by a Blade

D. Curtis Saunders and Jeffrey S. Marshall
School of Engineering, The University of Vermont
Burlington, Vermont, U.S.A.

Corresponding Author: Jeffrey S. Marshall, School of Engineering, The University of Vermont, Burlington, VT 05405, U.S.A. PHONE: 1 (802) 656-3826, EMAIL: jmarsha1@uvm.edu.

Keywords: vortex cutting; vortex reconnection; Burgers vortex sheet

Abstract

A computational study of vorticity reconnection, associated with the breaking and reconnection of vortex lines, during vortex cutting by a blade is reported. A series of Navier-Stokes simulations of vortex cutting with different values of the vortex strength are described, and the different phases in the vortex cutting process are compared to those of the more traditional vortex tube reconnection process. Each of the three phases of vortex tube reconnection described by Melander and Hussain (1989) are found to have counterparts in the vortex cutting problem, although we also point out numerous differences in the detailed mechanics by which these phases are achieved. Of particular importance in the vortex cutting process is the presence of vorticity generation from the blade surface within the reconnection region and the presence of strong vortex stretching due to the ambient flow about the blade leading edge. A simple exact Navier-Stokes solution is presented which describes the process by which incident vorticity is stretched and carried toward the surface by the ambient flow, and then interacts and is eventually annihilated by diffusive interaction with vorticity generated at the surface. The model combines a Hiemenz straining flow, a Burgers vortex sheet, and a Stokes first problem boundary layer, resulting in a nonlinear ordinary differential equation and a partial differential equation in two scaled time and distance variables that must be solved numerically. The simple model predictions exhibit qualitative agreement with the full numerical simulation results for vorticity annihilation near the leading edge stagnation point during vortex cutting.

1. Introduction

A blade approaching a vortex tube whose axis is oriented orthogonal to the blade leading edge will penetrate into the vortex core. In an inviscid fluid, Helmholtz's laws require that vortex lines remain material lines, and consequently the vortex tube will deform around the blade leading edge, but vortex lines originating within the vortex tube will remain within the tube (Marshall and Grant, 1996; Marshall, 2001). In a viscous fluid the Helmholtz restriction no longer applies, and vortex lines originating within the tube are observed to break and reconnect to vortex lines originating within the blade boundary layer (Liu and Marshall, 2004). The term *vorticity reconnection* refers to the topological change associated with vortex lines originating within the vortex tube breaking and reconnecting to vortex lines originating within a different vorticity region (Kida and Takaoka, 1994). The term *vortex cutting* refers to a specific type of vorticity reconnection process in which a solid object (such as the blade in the example above) passes through the vortex core, forcing vortex lines originating within the vortex tube to break and reconnect to those within the boundary layer of the solid object. Vortex cutting differs from traditional vortex reconnect problems by the fact that a vorticity generation surface (the surface of the solid body) lies in the reconnection region.

Vortex cutting is commonly observed when a propeller or airfoil blade passes through a vortex structure for cases where the blade width is small or on the same order as the vortex core diameter. In the canonical vortex cutting problem, the ambient vortex axis is orthogonal to the symmetry plane of the blade and the relative translation velocity of the blade and the vortex is in the direction of the blade chord (Coton et al., 2004). Vortex cutting is common in helicopter flows under slow flight conditions, where the

main rotor vortices are swept backward and chopped by the tail rotor (Leverton et al., 1977; Sheridan and Smith, 1980). The problem also arises in pumps, where intake vortices are cut by the pump impeller (Nagahara et al., 2001). In torpedo and submarine flow fields, the streamwise hull vortices and vortices shed from upstream control surfaces can become ingested into the propeller intake and cut by the propeller blades (Felli et al., 2009, 2011). Similarly in turbomachinary flows, upstream vortices shed from the stator blades are advected downstream and can be cut by the rotor blades (Binder, 1985), leading to enhanced turbulence generation. In cases where the vortex possesses a non-zero axial flow, vortex cutting events can lead to exertion of a sudden force on the blade, which can cause performance degradation, material fatigue or pitting (particularly in the presence of local cavitation), and noise and vibration generation (Ahmadi, 1986; Cary, 1987; Paterson and Amiet, 1979).

Vortex cutting is part of the more general process of orthogonal vortex-blade interaction, a review of which is given by Coton et al. (2004). A series of detailed experimental studies of orthogonal vortex-blade interaction and vortex cutting at high Reynolds number have been performed in the wind tunnel at Glasgow University using blade pressure measurements, flow visualization, and particle-image velocimetry (Doolan et al., 1999, 2001; Early et al., 2002; Green et al., 2000; Green et al., 2006; Wang et al., 2002). Experiments of vortex cutting in water at low Reynolds numbers have also been conducted, which allow for improved visualization using techniques such as laser-induced fluorescence, as reported by Johnson and Sullivan (1992), Krishnamoorthy and Marshall (1998), and Marshall and Krishnamoorthy (1997). The effect of vortex cutting on the ambient axial flow within the vortex core was examined using simplified

numerical and analytic models by Marshall (1994), Marshall and Yalamanchili (1994), Marshall and Krishnamoorthy (1997), and Lee et al. (1998) and experimentally by Krishnamoorthy and Marshall (1994). A key feature in many of these papers concerns wave motion induced on the vortex core by the sudden blocking of axial motion within the core during the vortex cutting process.

Detailed simulation of blade penetration into a vortex core was reported by Marshall and Grant (1996) for inviscid flow and by Liu and Marshall (2004) for viscous flow, in which the blade plane is oriented orthogonal to the vortex core at the point of impact. Cases with varying blade angle of attack were examined in viscous flow simulations by Filippone and Afgan (2008). These simulations exhibit a series of stages of the vortex cutting process. In the early stages of vortex cutting, as the blade leading edge is just starting to penetrate into the vortex core, the vortex responds in an almost inviscid fashion by reorienting the vortex lines originating within the vortex core to wrap around the blade leading edge. In the inviscid problem, the vortex lines within the vortex cannot be cut in accord with the second Helmholtz vortex law (Marshall, 2001), and they consequently bend around the blade leading edge and stretch, creating a strong vortex sheet (Marshall and Grant, 1996). In a viscous flow, the vorticity within the vortex near the leading edge diffusively interacts with vorticity of the opposite sign from the blade boundary layer, where the latter is generated both by the induced velocity along the blade span generated by the approaching vortex. The middle stage of vortex cutting is dominated by this diffusive cancellation of vorticity of opposite sign between the vortex core and the blade boundary layer, which is what allows vortex lines in the vortex to be

cut and to reconnect with vortex lines in the blade boundary layer, in a manner analogous to classic vortex reconnection problems (Kida and Takaoka, 1994; Saffman, 1990).

When the blade penetrates a sufficient distance into the vortex core, the spanwise velocity induced by the columnar vortex changes direction (Liu and Marshall, 2004). This change in spanwise velocity direction leads to a change in sign of the vorticity orthogonal to the blade plane at the blade leading edge, so that after this point the blade vorticity in this orthogonal direction is of the same sign as that within the vortex core and diffusive cancellation can no longer occur. As a result, the reconnection process between the vortex lines originating within the vortex core and those originating within the blade boundary layer is delayed, and the remaining parts of the vortex wrap around the blade leading edge in the form of a thin sheet, similar to what is observed in the inviscid problem. This situation constitutes the late stage of vortex cutting.

The objective of the current paper is to determine whether the same parameters and time scales govern the breaking and rejoining of vortex lines in both the vortex cutting problem and the classical vortex tube reconnection problem, and whether the different phases of the vortex reconnection problem (see, e.g., Kida and Takaoka, 1994, or Shelley et al., 1993) have analogues in the vortex cutting problem. This investigation is conducted using two different approaches. In the first approach, we conduct a series of high-resolution simulations of vortex cutting by a blade with no ambient axial flow within the vortex and with different values of the *impact parameter I*, defined in terms of the vortex-blade relative velocity U, the vortex core radius σ, and circulation Γ by $I = 2\pi\sigma U / \Gamma$. We examine temporal and spatial variation of pressure, vorticity, surface vorticity flux, and stretching and reconnection of vortex lines to understand how these

measures compare to similar measures in the literature on colliding vortex tubes. In the second approach, we present a highly simplified model that examines the vorticity diffusive cancellation process between an incident vortex (a stretched vortex sheet) and vorticity generated from a no-slip surface. The model is made analytically tractable by 'unwrapping' the blade surface, so that the vortex-blade interaction very close to the blade leading edge is represented by the problem of a stretched vortex sheet interacting with a flat surface in the presence of a straining flow. While this model is a bit too simplified to provide accurate quantitative comparison with the full Navier-Stokes vortex cutting simulation, as an exact Navier-Stokes solution it is useful for suggesting parameter scalings and for illustrating the physics of the vorticity cross-diffusion process in the presence of a no-slip surface.

We start with a brief review of classical vortex reconnection in Section 2, which is used to compare the vortex cutting results to classical vortex tube reconnection later in the paper. The numerical method used in the study is described in Section 3. Results of a series of numerical simulations with different impact parameter values are described in Section 4, with discussion of the similarities and differences between vortex cutting and vortex tube reconnection problems. In Section 5, we present a new exact Navier-Stokes solution that describes, in a qualitative way, some aspects of how the deformed impinging vortex interacts with the blade surface within the cutting region. Conclusions are given in Section 6.

2. Highlights of Vortex Reconnection

As described by Melander and Hussain (1989), vortex reconnection processes can be characterized by a series of three phases: 1) *inviscid induction*, which leads to alignment of the vortex cores into an anti-parallel formation (in which vortex axes are parallel with opposite axial vorticity sign) followed by core flattening and stretching, 2) *bridging* of the vortex cores, which occurs via cross-diffusion and cancelation of opposite-sign vorticity between the cores and subsequent linking of vortex lines, and 3) *threading*, or formation of fine threads from remnants of vorticity that have not yet completed reconnection before the cores are advected away from each other as a result of the high curvature of the reconnected vorticity sections.

In the first phase, two vortices driven towards each other will deform to adopt an anti-parallel configuration in the region near the reconnection position (Siggia, 1985). In many reconnection problems, the vortices are initially placed so that they will interact in this anti-parallel orientation, but in some cases, such as the problems of orthogonally offset vortices examined by Boratav et al. (1992) and Zabusky and Melander (1989), significant distortion of the vortices is required to attain the anti-parallel configuration. Once in this anti-parallel configuration, each vortex will induce a two-dimensional straining flow on the opposing vortex, and as a consequence the core of each vortex will become deformed and elongated. The curvature of the three-dimensional vortices along their axes both serves to drive the vortex cores into each other and to induce an additional background straining flow on the vortex pair which causes each deformed core to develop a *head-tail structure* (Kida et al., 1991). As shown in Figure 1a, the "head" is a region of increased thickness along the outside of the curved vortex core and the inner part of the core stretches out to become the "tail".

The second "bridging" phase of vortex reconnection is dominated by the diffusive cross-cancellation of vorticity between the two anti-parallel vortex cores. A simple model for this cross-cancellation process was proposed by Saffman (1990), the predictions of which were compared to results of numerical simulations by Shelley et al. (1993). As the opposite-sign vorticity cancels out due to diffusion between the two touching vortex cores, the vortex lines passing through the annihilated vorticity reconnect to those from the opposing vortex as a consequence of the requirement that the strength of a vortex tube remains uniform along the tube. These resulting bridges between the two vortex structures continue to grow stronger as more vorticity is diffusively annihilated within the vortex cores. However, since the vortex lines within these bridges are highly curved, their self-induced velocity increases as the bridges grow stronger, eventually causing them to propagate away from each other and discontinuing the vortex reconnection process before all vorticity within each vortex core has had a chance to diffusively interact with that in the opposing core.

The third phase of vortex reconnection deals with the remnants of vorticity, called threads, which are left behind as the bridges pull away from each other. As shown in Figure 1b, the threads have the form of a curved vortex pair, with a strength much less than that of the original vortex pair. The thread curvature is a result of both the self-induced velocity of the threads on each other and of the velocity induced by the bridges. The thread curvature leads to a weak self-induced velocity that drives the threads towards each other, but this motion is also influenced by the straining flow induced by the bridges. The velocity induced by the bridges also causes strong stretching of the threads, which intensifies the vorticity within the thread cores. As a consequence of these various

effects, the threads appear to remain in contact over a long time but the cross-diffusion between them is slow.

3. Numerical Model

The Navier-Stokes equations were solved in primitive-variable form using a finite-volume method (Lai, 2000) and a block-structured mesh with hexahedral elements. The domain consisted of four implicitly coupled blocks and was designed to achieve high spatial resolution along the leading edge of the blade and along the blade boundary layer (Figure 2). The simulation algorithm stores all dependent variables at the cell centers and calculates second-order accurate approximations of the diffusive and convective fluxes on the cell boundaries. The momentum and continuity equations are coupled together using the PISO algorithm (Issa, 1985). To achieve additional numerical stability, the time derivative is weighted between a second-order derivative approximation and a first-order upwind with a 90-10 ratio.

The computations were performed with a columnar vortex convected toward a fixed blade by a uniform upstream flow U. The Cartesian coordinate system used for these simulations was oriented such that the uniform flow was in the x-direction, the normal vector of the blade center plane was in the y-direction, and the blade span was in the z-direction (Figure 3). Standard inflow and outflow boundary conditions were used for the boundary planes in the x-direction, and symmetry boundary conditions were used in the y- and z-directions. The blade was a NACA0012 airfoil with chord length c and with leading edge lying on the line $x = 0$. The computational domain spanned the region $-3 \le x/c \le 3$, $-1 \le y/c \le 1$, and $-1.25 \le z/c \le 1.25$, where the blade center plane is

given by the intersection of the blade with the $y = 0$ plane. The initial velocity field was evaluated using a columnar Rankine vortex with uniform vorticity distribution, strength Γ, and core radius $\sigma_0 / c = 0.25$, along with two similar vortices in neighboring domains in the spanwise direction. The vortex axis was initialized on the central plane ($z_0 = 0$) at a location $x_0 / c = -1.1$ upstream of the blade leading edge, and the inlet plane was located upstream of the blade leading edge at $x_{inlet} / c = -3$.

Several dimensionless parameters can be defined which govern orthogonal vortex-blade interactions. The vortex and blade Reynolds numbers are defined as $\mathrm{Re}_V \equiv \Gamma / \nu$ and $\mathrm{Re}_B \equiv Uc / \nu$, where ν is the kinematic viscosity. The free-stream velocity U can be used to define the *impact parameter* as $I \equiv 2\pi\sigma_0 U / \Gamma$, which is the ratio of the relative vortex-blade velocity to the maximum swirl velocity within the vortex. The thickness parameter T / σ_0, which is the ratio of the blade thickness T to the vortex core radius σ_o, is important for determining the extent and type of vortex core deformation as the vortex approaches the blade. The ambient vortex axial flow was set to zero for all cases examined in the paper. The computations reported were selected to compare cases in the high impact parameter and low thickness parameter regime. The values of these parameters for the cases considered in the paper are given in Table 1. The thickness parameter is fixed at $T / \sigma_0 = 0.8$ and the blade Reynolds number is set at $\mathrm{Re}_B = 1000$ for all cases examined. The impact parameter varies from 0.5 to 20. In all instances, the impact parameter is sufficiently high that no separation of the boundary layer vorticity is observed prior to impact with the vortex. The vortex Reynolds number

varies inversely to the impact parameter, ranging from 79 to 3142 for the different cases examined.

Typical values of blade and vortex Reynolds numbers in vortex cutting problems depend upon the application. Taking helicopter flow as an example system, for instance, the typical blade Reynolds number Re_B is estimated by Leishman (2006) as about 5×10^6 for retreating blades and 2×10^7 for advancing blades. The typical vortex strength is estimated by Leishman as being approximately equal to the bound vortex strength on the blade surface, which for typical values of the blade solidity and thrust coefficient gives helicopter vortex Reynolds numbers Re_V of about 20% of the blade Reynolds number. While these Reynolds number values are much higher than those used in the current computations, it was shown by Liu and Marshall (2004), and is also the case for vortex reconnection problems in general, that the value of the Reynolds number has only a minor influence on the vortex cutting flow results. For instance, Liu and Marshall (2004) obtained computational results for blade lift coefficient during chopping of a vortex with axial flow which agree well with experimental values obtained at a Reynolds number three orders of magnitude higher than the computational value.

All length variables are non-dimensionalized using the blade chord *c*, velocity variables are non-dimensionalized by the free-stream velocity *U*, time is non-dimensionalized by the advective time c/U, and vorticity is non-dimensionalized by the inverse time scale U/c. Pressure and shear stress are non-dimensionalized by ρU^2, where ρ is the fluid density. The blade surface vorticity flux, defined by

$$\mathbf{q} = -\nu \frac{\partial \boldsymbol{\omega}}{\partial n}, \tag{1}$$

where **n** is the outward unit normal of the blade surface and ν is the kinematic viscosity, is non-dimensionalized by $\nu U / c^2$.

Grid independence was examined by repeating the calculation in Case 2 for four different meshes, where the total number of grid points varied by a factor of 4.5 between the coarsest and finest meshes. The meshes are labeled as mesh A (865,536 grid points), mesh B (1,900,701 grid points), and mesh C (3,883,238 grid points). All computations in this comparison were performed with the same parameter values and with the same computational domain size. Grid independence was demonstrated by computing the positive and negative circulation measures, defined by

$$\Gamma^+ = \int_L \omega_y^+ \, dx, \qquad \Gamma^- = \int_L \omega_y^- \, dx, \tag{2}$$

where $\omega_y^+ = \begin{cases} \omega_y & \text{if } \omega_y > 0 \\ 0 & \text{if } \omega_y \le 0 \end{cases}$ and $\omega_y^- = \begin{cases} 0 & \text{if } \omega_y > 0 \\ -\omega_y & \text{if } \omega_y \le 0 \end{cases}$. The line L lies on the blade symmetry plane, extending over the interval $-1.3 \le x \le 0$ upstream of the blade leading edge and passing through the ambient position of the vortex axis. The results are plotted as functions of time for each mesh type in Figure 4. The peak negative circulation measure has about 4% difference between meshes A and B, and less than 1% difference between meshes B and C. The peak positive circulation measure has about 10% difference between meshes A and B, and less than 5% difference between meshes B and

C. The negative values of ω_y lies within the vortex core and the positive values of ω_y are induced within the thin blade boundary layer at the leading edge in response to the induced velocity by the vortex, which explains why the positive circulation measure is more sensitive to grid resolution than is the negative circulation measure. All subsequent computations in the paper were performed using the grid in mesh C.

The effect of domain size was also considered to ensure the accuracy of the numerical simulations. The most important parameter was found to be the distance between the initial position of the vortex core and the inlet plane. If this distance was set too small, the induced velocity from the vortex caused weak positive *y*-vorticity to be generated on the inlet plane, which propagates towards the blade behind the vortex. When this vorticity reaches the blade leading edge it diffusively cancels with the uncut portion of the vortex core that was stretched around the blade leading edge. Several domains were examined, and the mesh in Figure 2 was chosen in order to ensure that the strength of this inlet vorticity was small and that it did not reach the blade until very late in the computation. In addition, the effect of time step was considered and a dimensionless time step of 0.015 was chosen to ensure a CFL number of less than unity.

4. Vortex Cutting Simulation Results

The ambient vorticity within the vortex is in the negative *y* direction. As the vortex approaches the blade, it induces a spanwise velocity which is associated with generation of vorticity in the positive *y* direction along the blade leading edge. It is the diffusive cross-cancellation of the *y*-oriented vorticity within the vortex with that in the boundary layer along the blade leading edge that controls the vortex cutting process,

through which vortex lines within the vortex are cut and reconnect to vortex lines within the blade boundary layer. Results of numerical simulations of the vortex cutting process at different values of the impact parameter, as listed in Table 1, are presented in this section.

4.1. Vorticity Dynamics during Vortex Cutting

Throughout this section detailed results are shown for Case 2, and then comparisons of selected results for computations at other values of the impact parameter are given in Section 4.2. A timeline of the basic vortex cutting process is given in Figure 5, in which contour plots of ω_y are shown in the *x*-*y* plane for three times to illustrate the position of the vortex core relative to the blade during different phases of the vortex cutting process. A close-up plot is given in Figure 6, showing the ω_y values within a region near the blade leading edge, where regions with high negative values of ω_y are shown in blue and regions with high positive values of ω_y are shown in red. At the beginning stage of cutting, the vortex induces a region of positive ω_y within the blade leading edge boundary layer. As the vortex impacts onto the blade, the regions with positive and negative values of ω_y, within the blade boundary layer and the vortex core, respectively, interact by diffusion and partially annihilate each other. This leads to a rapid decrease in both the negative and positive circulation measures, as shown in Figure 4 between times of about $t = 0.5$ and 1.0, and causes the vortex lines in the vortex core to break and reconnect to those in the blade boundary layer. However, it is clear that from about the third frame of the series in Figure 6 onward in time, the value of ω_y within the

blade boundary layer has changed from positive to negative. As demonstrated by Liu and Marshall (2004), this change in sign is associated with the fact that as the blade leading edge passes through the core, the induced spanwise velocity along the leading edge changes direction. After the change in sign of ω_y within the blade boundary layer occurs, the *y*-component of vorticity within the core is of the same sign as that within the blade boundary layer and diffusive annihilation can no longer occur. A series of plots showing how the value of ω_y along the blade leading edge changes sign is given in Figure 7, for a similar time frame as in Figure 6 but viewed looking along the *x*-direction, directly toward the blade front region. From this figure, we see that the change in sign of ω_y first occurs at the ends of the blade span and then moves toward the blade center as time progresses.

The *x*-component of vorticity also undergoes a sign change as the vortex core passes over the leading edge of the blade. Initially, the induced spanwise velocity from the vortex causes a region of positive ω_x to form on the blade top and a region of negative ω_x on the blade bottom. As the vortex passes over a given point on the blade surface, the induced spanwise velocity at that point changes direction, resulting in a change in the sign of ω_x. Plots illustrating this effect using a time series of contours of ω_x are shown on the cross-sectional plane $z = 0$ (Figure 8) and on projections of the blade top and bottom surfaces looking along the *y*-axis (Figure 9). The change in sign of ω_x closely follows the path of the vortex core.

The essence of vortex reconnection involves cutting of vortex lines originating from one vorticity region and reconnection to vortex lines originating from another

vorticity region via diffusion-regulated annihilation of vorticity between the two regions. This vortex line reconnection process for the vortex cutting problem is illustrated in Figure 10 for three times as the blade penetrates into the vortex core. In order to illustrate the vortex reconnection process, we color the vortex lines green to indicate vortex lines that originate within the vortex and remain within the vortex, black to indicate vortex lines that originate within the blade boundary layer and remain within the boundary layer, and red to indicate vortex lines that originate within the vortex and cross over to join those within the blade boundary layer (or vice versa). At the first time (Figure 10a), the blade leading edge has penetrated about 30% of the way through the vortex core. At this stage, the sign of ω_y is positive at the blade leading edge and vorticity annihilation between the boundary layer and the vortex allows the vortex lines within the core to cut and reconnect to those within the boundary layer. At the second time (Figure 10b), the vortex core center has just passed the position of the blade leading edge and the value of ω_y at the leading edge is in the process of changing sign. Vortex lines from the vortex (in green) are now beginning to deform and to be stretched in the spanwise direction instead of being cut. This process continues in Figure 10c, where the green vortex lines are clearly deforming and stretching in the *z*-direction (spanwise) rather than being cut. Also, the pattern change of the black vortex lines illustrates how the vorticity orientation in the boundary layer along the front section of the blade changes as the vortex core passes over the blade leading edge.

The pressure change along the vortex core caused by the presence of the blade is another important aspect of the vortex cutting process. For reconnection of two anti-parallel vortex tubes, Saffman (1990) proposed that the localized increase in vortex core

pressure creates a positive feedback loop to drive the vortex reconnection process. We examined how the pressure in the vortex core changed for vortex cutting in order to understand if pressure plays a similar role in the vortex cutting problem. Figure 11 illustrates the pressure in the vortex core for a contour plot in the $z = 0$ plane, passing through the center span of the blade. Initially there is a large region of low pressure in the vortex core as well as on the top and bottom surfaces of the blade and a region of high pressure around the blade leading edge. As the vortex moves closer to the blade, the pressure in the vortex core increases close to the impingement region and a pressure gradient forms. This phenomenon is similar to the one Saffman (1990) described, but it occurs for a different reason. In the case of vortex cutting by a blade, the impingement of the vortex upon the ambient high pressure near the blade leading edge no doubt plays a significant role in driving the localized pressure gradient along the vortex core, and any role that core deformation might play in this process is obscured. As the vortex passes over the blade, the low pressure region in the vortex core connects with the low pressure regions on the top and bottom surfaces of the blade, as shown in Figures 11c and d.

The key difference between vortex cutting by a blade and more traditional vortex reconnection is the fact that vorticity is generated on the blade surface, which lies within the region dominated by vorticity diffusive interaction. The *x* and *y* components of the surface vortex flux, q_x and q_y, are shown within a projection the front region of the blade (looking along the *x*-axis) in Figures 12 and 13. The vorticity flux contour plots exhibit a change in sign around t = 1.05, which corresponds with the change in sign of ω_x and ω_y during vortex passage previously discussed in this section. The contour plots show that the vorticity flux is primarily generated within the leading edge region of the

blade, and not on the blade top and bottom surfaces away from the leading edge. This region is exactly where the breaking and rejoining of vortex lines occurs, and further demonstrates the importance of considering the role of surface vorticity flux in a blade-vortex cutting problem.

4.2. Effect of Impact Parameter

Time variation of the maximum and minimum values of vorticity and surface vorticity flux are plotted for all four cases examined in Figures 14 and 15 in order to better understand the effect of impact parameter on the temporal changes in these quantities throughout the vortex cutting process and the manner in which the vortex cutting process changes with respect to the impact parameter. In interpreting these plots, it is helpful to keep in mind the time intervals for major transitions in the cutting process, namely, the onset of penetration of the blade leading edge into the vortex core ($t \cong 0.45$), the passage of the blade leading edge out of the opposite side of the vortex position ($t \cong 1.2$), and stretching of vortex remnants over the blade leading edge ($t > 1.2$). These three time intervals correspond approximately to the three phases of traditional vortex tube reconnection as described in Section 2.

Figure 14 shows the time variation of the maximum values of ω_x and ω_z, normalized with respect to the vortex Reynolds number Re_V. The minimum values of these vorticity components follow nearly identical profiles as the maximum values due to the symmetry on the top and bottom surfaces of the blade, and so are not plotted. The different cases considered differ from each other by the value of the vortex strength, leading to different values of the vortex Reynolds number and vortex-blade impact

parameter. However, the plots of maximum and minimum normalized ω_x values for these different cases appear to nearly collapse onto a single curve, although with a slight deviation for Case 1. The plot in Figure 14a exhibits an increase in ω_x with time until around t = 0.75, which corresponds to the time at which the vortex core axis passes over the blade leading edge. Following this time, the value of ω_x gradually decreases until it approaches its initial value as the vortex moves past the tail end of the blade. The maximum value of ω_x occurs in the center of the blade, slightly above the blade centerplane but within the blade boundary layer. From Figure 14a, we conclude that the maximum value of ω_x is dominated by the initial cutting of the vortex, and that this value increases approximately linearly with the vortex strength.

The maximum value of ω_z / Re_V, shown in Figure 14b, clearly does not collapse onto a single curve for the different cases examined. The results for the different cases appear to be qualitatively similar, but the maximum value of ω_z / Re_V increases/decreases as the vortex Reynolds number increases/decreases. The maximum in ω_z also occurs at a somewhat later time than does the maximum in ω_x, although it seems to occur at the same time for all of the cases examined. In contrast to the maximum of ω_x, the maximum value of ω_z occurs to the left of the center of the blade span and slightly below the blade center plane. This shift is likely due to the induced velocity of the vortex creating a slightly higher free-stream velocity on the left side of the blade and slightly lower velocity on the right side, looking downwind toward the blade leading edge.

The maximum and minimum values of ω_y, normalized by the vortex Reynolds number, are plotted in Figures 14c and 14d for the four cases listed in Table 1, each with different value of the impact parameter. We again see that the curves nearly coincide for the different cases examined, with the exception of a slight deviation for Case 1. This data collapse indicates that the value of ω_y varies approximately linearly with vortex strength. The maximum positive value of ω_y (which occurs within the boundary layer at the blade leading edge) initially increases as the blade penetrates into the vortex core until a time of about t = 0.75, and after which it decreases to a value of nearly zero as the vortex core passes over the leading edge of the blade and the positive vorticity on the blade front induced by the vortex changes sign. The maximum negative value of ω_y, which initially occurs within the vortex core, exhibits a gradual decay with time during the initial part of the computation, which is due to viscous diffusion of the vortex core. The maximum negative value of ω_y is not significantly effected by the vortex cutting process until the vortex core moves past the blade leading edge and the value of ω_y within the blade boundary layer changes from a positive to a negative sign. From this time until the end of the computation, the point of maximum negative value of ω_y is located at the blade leading edge. The maximum negative value of ω_y gradually increases from the time (t = 0.75) of change in sign of ω_y within the blade boundary layer to a time at which the blade leading edge has entirely penetrated through the vortex core (about $t = 1.5$), after which the maximum negative value of ω_y remains approximately constant for the remainder of the computation. Both the generation of

negative ω_y due to induced spanwise velocity from the vortex and the increase in vorticity due to stretching of the remaining portions of the vortex wrapped about the blade leading edge contribute to producing the maximum negative ω_y value. The fact that the peak value of the maximum negative value of ω_y occurs quite late, when the vortex core is well past the center of the blade, suggests the presence of significant uncut vorticity remnants from the impinging vortex. These uncut vorticity remnants wrap around the blade surface in the form of a thin vortex sheet, for which the value of the negative vorticity component ω_y continuously intensifies by stretching about the blade leading edge while at the same time it is regulated by viscous diffusion, eventually approaching a constant value in a manner analogous to the classical Burgers vortex (Burgers, 1948).

The time variation in positive and negative components of the surface vorticity flux is shown in Figure 15. The *x*- and *z*-vorticity fluxes, q_x and q_z, exhibit a functional form very similar to the corresponding maximum values of the vorticity components ω_x and ω_z. As was the case for the vorticity, the maximum positive and negative values of the vorticity flux in these directions follow the same curve, and the maximum values of q_x for the different cases examined collapse nearly onto a single curve while those for q_z do not. We again see an initial increase in the positive vorticity flux component q_y which then drops off to 0 as the cutting process stops, and a late increase in the negative component of vorticity flux as negative *y*-vorticity is generated on the blade leading edge.

To conclude this section, we return to the discussion in Section 2 of the different physical processes that occur during vortex reconnection, and compare these processes to

those occurring during vortex cutting. We had identified three distinct phases of vortex reconnection. The first phase is dominated by inviscid interaction of the vortices and has two parts - anti-parallelization and core deformation. The vortex cutting process appears at first view to be most similar to the orthogonally-offset vortex reconnection problem, of the type examined by Boratav et al. (1992) and Zabusky and Melander (1989), since the ambient blade boundary layer vorticity is in the *z*-direction and the ambient vorticity within the vortex is in the *y*-direction. However, unlike in the orthogonal vortex tube reconnection problem, the impinging vortex does not twist around to orient itself anti-parallel to the ambient boundary layer vorticity as it approaches the blade. Instead, the induced velocity from the vortex generates new vorticity in the anti-parallel direction to the incident vortex on the blade leading edge as the vortex approaches. Instead of an inviscid vortex twisting process, in the vortex cutting case the anti-parallel configuration is achieved via viscous vorticity generation on the blade surface. The extent of inviscid core deformation in the vortex cutting process depends greatly on the value of the thickness parameter, T/σ_0. For sufficiently large values of this parameter, significant core deformation can occur as the impinging vortex interacts inviscidly with its image over the blade surface.

The second phase of vortex reconnection entails viscous annihilation of anti-parallel vorticity between the two vorticity regions, leading to vortex line cutting and reconnection between the regions. This process occurs much the same in the vortex tube reconnection and vortex cutting problems, with the difference that in classical vortex tube reconnection all of the vorticity is present at the start of the computation, whereas for

vortex cutting vorticity is continually being generated at the blade surface during the reconnection process.

Both the classical vortex tube reconnection and the vortex cutting processes are incomplete, leading to the formation of uncut remnants, or threads, in the third phase of reconnection. Despite this similarity, the reasons that the vortex tube reconnection and the vortex cutting are incomplete are quite different. For vortex tube reconnection, the incomplete reconnection occurs due to the velocity induced by the highly curved bridge regions connecting the two vortex tubes. As these bridges grow in strength, the self-induced velocity gets larger and it is eventually sufficient to move the cores away from one another before all opposite-sign vorticity in the reconnection region has been annihilated. For the vortex cutting process, the incomplete cutting occurs due to the change in sign of the vorticity flux in the anti-parallel (y) direction on the blade leading edge as the leading edge penetrates sufficiently far into the vortex core. Regardless of the different mechanism leading to incomplete reconnection, the end result for both processes is the formation of uncut vorticity threads that linger for long time periods after the primary reconnection or cutting process is complete.

5. Model for Vortex Sheet in a Straining Flow near a Surface

A key component of the vortex cutting process involves diffusive vorticity annihilation between the incident vortex and vorticity generated on the blade boundary layer. The incident vorticity initially has the form of a tube, but as it wraps about the blade leading edge it deforms into more of a sheet-like structure (Marshall and Grant, 1996). Finally, the stretching of the impinging vortex imposed by the ambient flow about

the blade leading edge plays a critical role in determining the vorticity evolution within the cutting region. In this section we describe a new exact Navier-Stokes solution that contains these three elements – anti-parallel vorticity diffusive annihilation, vorticity generation on a surface, and vortex stretching. While the model to be presented incorporates these three key elements, to make the problem analytically tractable, we must dramatically modify certain other elements of the vortex cutting problem. In particular, the model does not deal with vorticity bending around the highly curved blade leading edge, but instead considers vorticity above a flat surface that is stretched by an imposed viscous straining flow (Hiemenz, 1911), as indicated in the schematic diagram in Figure 16. Secondly, the vortex sheet is assumed to be infinitely wide, whereas the incident vortex in the vortex cutting problem has a finite width. Were it not for the presence of the solid surface, this stretched vortex sheet would be identical to a Burgers sheet, where the vorticity within the sheet is oriented along the direction of the straining flow (Burgers, 1948; Gibbon et al., 1999). Because of these various simplifications incorporated into the model, we do not expect the model solutions to provide an accurate quantitative approximation of the vorticity field in the problem of vortex cutting by a blade. Nevertheless, the model contains many of the key ingredients of the vortex cutting problem and it may be helpful in suggesting physically-motivated scaling for the vortex cutting problem. As an exact Navier-Stokes solution, the model is also of interest in its own right.

The model deals with a combination of a Hiemenz straining flow and a vortex sheet over a flat surface. The model problem is solved using the Cartesian coordinate system $(\hat{x},\hat{y},\hat{z})$ shown in Figure 16, in which $\hat{z}$ points in the upstream direction, $\hat{x}$ is

oriented in the direction of the Heimenz straining flow close to the wall, and $\hat{y}$ is in the direction of the flow induced by the vortex sheet. Figure 16 illustrates the fact that this model is not intended to be representative of the entire vortex-blade interaction problem, but only of the flow very close to the point of vortex impingement on the blade leading edge. The velocity and pressure fields are assumed to satisfy

$$\mathbf{u} = \hat{u}(\hat{x},\hat{z})\mathbf{e}_{\hat{x}} + \hat{v}(\hat{z},t)\mathbf{e}_{\hat{y}} + \hat{w}(\hat{z})\mathbf{e}_{\hat{z}}, \qquad p = p_1(\hat{x}) + p_2(\hat{z}). \tag{3}$$

Under these conditions the continuity and Navier-Stokes equations reduce to

$$\frac{\partial \hat{u}}{\partial \hat{x}} + \frac{\partial \hat{w}}{\partial \hat{z}} = 0, \tag{4a}$$

$$\hat{u}\frac{\partial \hat{u}}{\partial \hat{x}} + \hat{w}\frac{\partial \hat{u}}{\partial \hat{z}} = -\frac{1}{\rho}\frac{\partial p_1}{\partial \hat{x}} + \nu\left(\frac{\partial^2 \hat{u}}{\partial \hat{x}^2} + \frac{\partial^2 \hat{u}}{\partial \hat{z}^2}\right), \tag{4b}$$

$$\frac{\partial \hat{v}}{\partial t} + \hat{w}\frac{\partial \hat{v}}{\partial \hat{z}} = \nu\,\frac{\partial^2 \hat{v}}{\partial \hat{z}^2}, \tag{4c}$$

$$\hat{w}\frac{\partial \hat{w}}{\partial \hat{z}} = -\frac{1}{\rho}\frac{\partial p_2}{\partial \hat{z}} + \nu\,\frac{\partial^2 \hat{w}}{\partial \hat{z}^2}. \tag{4d}$$

We denote the straining rate of the external Hiemenz flow by *s*, the strength of the Burgers vortex sheet by γ, a scaled height variable by $\eta = \hat{z}\sqrt{s/\nu}$, and a scaled time by $\tau = st$. The velocity components can be written as

$$\hat{u} = s\hat{x}F'(\eta), \qquad \hat{v} = \gamma\, G(\eta,\tau), \qquad \hat{w} = -F(\eta)\sqrt{s\nu}. \tag{5}$$

These expressions for velocity satisfy the continuity equation (4a) identically, and the momentum equations (4b) and (4d) reduce to an ordinary differential equation for $F(\eta)$ as

$$F''' + FF'' - (F')^2 + 1 = 0, \tag{6}$$

subject to the boundary conditions $F(0) = F'(0) = 0$ and $F'(\infty) = 1$. Substituting (5) into (4c) yields a partial differential equation for $G(\eta, \tau)$ as

$$\frac{\partial G}{\partial \tau} - F(\eta)\frac{\partial G}{\partial \eta} = \frac{\partial^2 G}{\partial \eta^2}. \tag{7}$$

Equation (7) is subject to the boundary conditions

$$G(0, \tau) = 0, \quad G(\infty, \tau) = \alpha, \tag{8}$$

where α is a prescribed parameter representing the ratio of the velocity far away from the plate to the vortex sheet strength.

Equation (6) is the equivalent to the classic Hiemenz problem, which was solved using a fourth-order Runge-Kutta method, yielding $F''(0) = 1.23259$. Equation (7) was solved using the Crank-Nicholson method with $\Delta\eta = 0.005$ and $\Delta\tau = 0.001$. The primary dimensionless parameter is the ratio α of velocity $\hat{v}_\infty$ in the $\hat{y}$-direction far away from the surface to the initial vortex sheet strength γ. Other parameters include the

initial position η_0 of the vortex sheet and the initial thickness Δ of the Stokes first problem boundary layer on the wall. A simple example calculation is considered using this model for the problem of a vortex sheet being driven into a flat wall by a Hiemenz straining flow. The initial condition for this example problem has the form of an equilibrium Burgers vortex sheet centered at η_0 and a Stokes first problem boundary layer with dimensionless thickness Δ, given by

$$G(\eta,0) = G_0(\eta) = (1+\alpha)\mathrm{erf}(\eta/2\Delta) - \frac{1}{2} - \frac{1}{2}\mathrm{erf}[(\eta-\eta_0)/\sqrt{2}], \qquad (9)$$

where erf(·) is the error function. For this example problem, we chose $\eta_0 = 10$ and $\Delta = 1$. Results for this flow are shown in Figure 17 for the dimensionless velocity $G = \hat{v}/\gamma$ and dimensionless vorticity $\zeta \equiv \partial G/\partial\eta$ as functions of dimensionless time τ. Based on the coordinate system shown in Figure 16, the velocity is in the $\hat{y}$-direction and the vorticity is in the $\hat{x}$-direction. Dimensionless circulation measures Γ^+ and Γ^- are defined by

$$\Gamma^+ = \int_L \zeta^+ \, d\eta, \qquad \Gamma^- = \int_L \zeta^- \, d\eta, \qquad (10)$$

where $\zeta^+ = \begin{cases} \zeta & \text{if } \zeta > 0 \\ 0 & \text{if } \zeta \le 0 \end{cases}$ and $\zeta^- = \begin{cases} 0 & \text{if } \zeta > 0 \\ -\zeta & \text{if } \zeta \le 0 \end{cases}$, and L denotes the range $(0,\eta_{\max})$ of η. Plots of time variation of Γ^+ and Γ^-, given for the example problem in Figure 18, provide a quantitative measure of the extent of vorticity diffusion-driven annihilation occurring between the incident vortex sheet and the boundary layer vorticity.

In the numerical simulation of vortex cutting by a blade discussed in Section 4, the assumption that the ambient flow past the blade has the form of a plane straining flow would only be relevant in a region close to the blade leading edge. While we do not expect this simple model to provide an accurate quantitative description of the full numerical simulation, it is nevertheless of interest to compare the model results with those of the full numerical simulation within this near-blade region. In comparing these result, we note the relationships $(\hat{x},\hat{y},\hat{z}) = (y,-z,-x)$ and $(\hat{u},\hat{v},\hat{w}) = (v,-w,-u)$ between coordinate and velocity components in the model problem and the numerical simulation. The value of the spanwise velocity component w was extracted from the numerical simulations along a line corresponding with the -x axis from $x = 0$ to $x = -15\sqrt{s/\nu}$, corresponding to the interval $0 \le \eta \le 15$. The straining rate s was obtained by extracting the velocity component v in the y-direction along this same line and fitting a tangent line near $\eta = 0$, which for Case 2 yields $s = 26.7$. The negative spanwise velocity $(-w)$ extracted along this line is comparable to the velocity component $\hat{v}$ in the simple theoretical model, and it is plotted as a function of η in Figure 19a for different values of the scaled time variable $\tau = st$. Comparison results for the theoretical model were obtained using the same initial velocity profile as shown in Figure 18a for the vortex cutting simulation, and by varying the boundary condition α in (8) as a function of time in accordance with the values of $\hat{v}$ at the position $\eta = 15$ along the extraction line obtained from the vortex cutting simulation. The model calculation was initialized at $\tau = 8$ in order to give the vortex time to approach the blade surface. The results from the model calculations are plotted in Figure 19b for the velocity profile. The two sets of results do not exactly match up, but they have sufficiently good qualitative similarities to

suggest that the temporal and spatial scaling suggested by the model are valid also with more general vortex cutting problem. To quantify the vorticity annihilation in the vortex cutting simulations and the simple model, we plot in Figure 20 the time variation of the positive and negative circulation measures Γ^+ and Γ^-, which are computed in this case using integration over the interval $0 \le \eta \le 15$, corresponding to the interval $-0.09 \le x \le 0$ in the numerical simulations of vortex cutting by a blade. We observe higher peaks of both the positive and negative circulation for the vortex cutting simulations compared to the simple model, which is likely an effect of the strong curvature of the vortex around the blade leading edge in the vortex cutting simulations. The qualitative features of the two plots, including the vorticity variation on the time scale τ and the manner in which the stretched vorticity within the flow interacts and is annihilated by vorticity generated at the surface, appear to be similar between the model and the full simulations.

6. Conclusions

Computational results are reported for the cutting of a columnar vortex by a blade without axial flow for different values of the impact parameter, with a particular focus on comparison of the vortex cutting problem to the classic vortex tube reconnection problem. Each of the three phases of vortex tube reconnection were found to have a close analogy in the vortex cutting problem. The first vortex reconnection phase, involving inviscid response to the core resulting in both anti-parallel orientation of the vorticity and core shape deformation, takes the form in the vortex cutting problem of generation of vorticity at the leading edge of the blade due to the spanwise velocity induced by the impinging vortex. While the diffusion of this vorticity into the blade boundary layer is a

viscous process, the generation of vorticity at the blade surface is controlled by the inviscid slip velocity along the blade span. The resulting vorticity within the boundary layer wrapping about the blade leading edge is anti-parallel to that within the approaching vortex core.

The second phase of vortex reconnection involves diffusion and annihilation of vorticity within the two anti-parallel vorticity regions. This process occurs in the vortex cutting problem between the vortex core and the boundary layer at the blade leading edge. However, unlike the traditional vortex tube reconnection problem, for vortex cutting the boundary layer vorticity is generated at the blade surface as the vorticity annihilation occurs. A simple exact Navier-Stokes solution illustrating the key processes involved during this second phase of vortex cutting is described in Section 5, in which we examine the interaction of a vortex sheet above a flat surface in the presence of a straining flow. In this model, the straining flow is in the direction of the vorticity vectors, similar to a Burgers' vortex, and represents the effect of the ambient flow in the stagnation-point region near the blade leading edge. While this model is greatly simplified in order to reduce the problem to a manageable form, and in particular the effect of high curvature at the blade leading edge is ignored, it nevertheless is found to provide a good description of the qualitative features of vortex cutting and to indicate the appropriate temporal and spatial scaling for the problem.

Both the vortex tube reconnection problem and the vortex cutting problem result in incomplete reconnection of the vortex lines across the two vorticity regions; however, the reason that this occurs in the two problems is different. In vortex cutting, the incomplete cutting occurs when the blade leading edge passes sufficiently deeply into the

vortex core that the induced spanwise velocity along the leading edge changes sign. After this sign change occurs, the generation of anti-parallel vorticity at the leading edge surface is stopped and the new vorticity generated is parallel to that within the vortex core. When the anti-parallel vorticity in the boundary layer is depleted and replaced by parallel vorticity, the diffusive annihilation of vorticity between the vortex and the boundary layer can no longer occur, effectively stopping the vortex cutting process. What follows corresponds with the third phase of vortex reconnection, in which remnants of the uncut vortex remain for long time, wrapping around the blade boundary layer and stretching under the influence of the ambient flow around the blade.

Acknowledgements

We gratefully acknowledge support of this work from the National Science Foundation under project DGE-1144388.

References

Ahmadi, A. R. 1986 An experimental investigation of blade-vortex interaction at normal incidence. *AIAA Journal of Aircraft* **23**(1), 47-55.

Binder, A. 1985 Turbulence production due to secondary vortex cutting in a turbine rotor. *Journal of Engineering for Gas Turbines and Power* **107**, 1039-1046.

Boratav, O. N., Pelz, R. B. & Zabusky, N. J. 1992 Reconnection in orthogonally interacting vortex tubes: Direct numerical simulations and quantifications. *Physics of Fluids A* **4**(3), 581-605.

Burgers, J. M. 1948 A mathematical model illustrating the theory of turbulence. *Adv. Appl. Mech.* **1**, 171–199.

Cary, C. M. 1987 An experimental investigation of the chopping of helicopter main rotor tip vortices by the tail rotor. NASA CR-177457.

Coton, F. N., Marshall, J. S., McD. Galbraith, R. A. & Green, R. B. 2004 Helicopter tail rotor orthogonal blade-vortex interaction. *Progress in Aerospace Sciences* **40**(7), 453-486.

Doolan, C., Coton, F. & Galbraith, R. 1999 Three-dimensional vortex interactions with a stationary blade. *Aeronautical Journal* **103**(1030), 578-587.

Doolan, C.J., Coton, F.N. & Galbraith, R.A. 2001 Surface pressure measurements of the orthogonal vortex interaction. *AIAA Journal* **38**(1), 88-95.

Early, J., Green, R. & Coton, F. 2002 Flow visualization of the orthogonal blade-vortex interaction using particle image velocimetry. *Aeronautical Journal* **106**(1057), 137-145.

Felli, M. & Falchi, M. 2011 Propeller tip and hub vortex dynamics in the interaction with a rudder. *Experiments in Fluids* **51**, 1385-1402.

Felli, M., Roberto, C. & Guj, G. 2009 Experimental analysis of the flow field around a propeller-rudder configuration. *Experiments in Fluids* **46**, 147-164.

Filippone, A. & Afgan, I. 2008 Orthogonal blade-vortex interaction on a helicopter tail rotor. *AIAA Journal* **46**(6), 1476-1489.

Gibbon, J. D., Fokas, A. S. & Doering, C. R. 1999 Dynamically stretched vortices as solutions of the 3D Navier–Stokes equations. *Physica D* **132**, 497–510.

Green, R., Doolan, C. & Cannon, R. 2000 Measurements of the orthogonal blade-vortex interaction using a particle image velocimetry technique. *Experiments in Fluids* **29**, 369-379.

Green, R. B., Coton, F. N. & Early, J. M. 2006 On the three-dimensional nature of the orthogonal blade-vortex interaction. *Experiments in Fluids* **41**, 749-761.

Hiemenz, K. 1911 Die Grenzschicht an einem in den gleichförmigen Flüssigkeitsstrom eingetauchten geraden Kreiszylinder. *Dingler's Polytech. J.* **326**, 321.

Issa, R. 1985 Solution of the implicit discretized fluid flow equations by operator splitting. *Journal of Computational Physics* **62**, 40-65.

Johnston, R. T. & Sullivan, J. P. 1992 Unsteady wing surface pressures in the wake of a propeller. AIAA Paper 92-0277.

Kida, S., Takaoka, M. & Hussain, F. 1991 Formation of head-tail structure in a two-dimensional uniform straining flow. *Physics of Fluids A* **3**(11), 2688-2697.

Kida, S. & Takaoka, M. 1994 Vortex reconnection. *Annual Review of Fluid Mechanics* **26**, 169-189.

Krishnamoorthy, S. & Marshall, J.S. 1994 An experimental investigation of 'vortex shocks'. *Physics of Fluids* **6**(11), 3737-3741.

Krishnamoorthy, S. & Marshall, J.S. 1998 Three-dimensional blade-vortex interaction in the strong-vortex regime. *Physics of Fluids* **10**(11), 2828-2845.

Lai, Y.G. 2000 Unstructured grid arbitrarily shaped element method for fluid flow simulation. *AIAA Journal* **38**(12), 2246-2252.

Lee, J., Burggraf, O. & Conlisk, A. 1998 On the impulsive blocking of a vortex jet. *Journal of Fluid Mechanics* **369**, 301-331.

Leishman, J. G., *Principles of Helicopter Aerodynamics*, Cambridge University Press, Cambridge, U.K., p. 351 (2006).

Leverton, J. W., Pollard, J. S. & Wills, C. R. 1977 Main rotor wake/tail rotor interaction. *Vertica* **1**, 213-221.

Liu, X. & Marshall, J.S. 2004 Blade penetration into a vortex core with and without axial core flow. *Journal of Fluid Mechanics* **519**, 81-103.

Marshall, J. S. 1994 Vortex cutting by a blade. Part I. General theory and a simple solution. *AIAA Journal* **32**(6), 1145-1150.

Marshall, J. S., *Inviscid Incompressible Flow*, John Wiley & Sons, New York (2001).

Marshall, J. S. & Grant, J. R., 1996 Penetration of a blade into a vortex core: vorticity response and unsteady blade forces. *Journal of Fluid Mechanics* **306**, 83-109.

Marshall, J. S. & Krishnamoorthy, S. 1997 On the instantaneous cutting of a columnar vortex with non-zero axial flow. *Journal of Fluid Mechanics* 351, 41-74.

Marshall, J. S. & Yalamanchili, R. 1994 Vortex cutting by a blade. Part II. Computations of vortex response. *AIAA Journal* **32**(7), 1428-1436.

Melander, M. V. & Hussain, F. 1989 Cross-linking of two antiparallel vortex tubes. *Physics of Fluids A* **1**(4), 633-635.

Nagahara, T., Sato, T. & Okamura, T. 2001 Effect of the submerged vortex cavitation occurred in pump suction intake on hydraulic forces of mixed flow pump impeller. CAV 2001: 4th International Symposium on Cavitation, Pasadena, California.

Paterson, R. W. & Amiet, R. K. 1979 Noise of a model helicopter rotor due to ingestion of turbulence. NASA Tech. Rept. NASA CR-2313.

Saffman, P. G. 1990 A model of vortex reconnection. *Journal of Fluid Mechanics* **212**, 395-402.

Shelley, M. J., Meiron, D. I. & Orszag, S. A. 1993 Dynamical aspects of vortex reconnection of perturbed anti-parallel vortex tubes. *Journal of Fluid Mechanics* 246, 613-652.

Sheridan, P. F. & Smith, R. P. 1980 Interactional aerodynamics – a new challenge to helicopter technology. *Journal of the American Helicopter Society* **25**(1), 3-21.

Siggia, E. D. 1985 Collapse and amplification of a vortex filament. *Physics of Fluids* **28**, 794-805.

Wang, T., Doolan, C. J., Coton, F. N. & Galbraith, R. A. M. 2002 Experimental study of the three-dimensionality of orthogonal blade-vortex interaction. *AIAA Journal* **40**(10), 2037-2046.

Zabusky, N. J. & Melander, M. V. 1989 Three-dimensional vortex tube reconnection: morphology for orthogonally-offset tubes. *Physica D* **37**, 555-562.

List of Figures

Figure 11. Pressure contours in the *x*-*y* plane passing through the center span of the blade for (a) t = 0.3, (b) 0.6, (c) 0.9, and (d) 1.2. The outlines of the vortex are shown by plotting vortex lines on the two sides of the vortex.

Figure 12. Contour plots of the *x* component of the vorticity flux, q_x, on blade leading edge, at times (a) t = 0.45, (b) 0.75, (c) 1.05, and (d) 1.35.

Figure 13. Contour plots of the *y* component of the vorticity flux, q_y, on the blade leading edge, at times (a) t = 0.45, (b) 0.75, (c) 1.05, and (d) 1.35.

Figure 14. Time variation of (a) maximum ω_x, (b) maximum ω_z, (c) maximum ω_y, and (d) minimum ω_y, normalized with respect to the vortex Reynolds number $\mathrm{Re}_V = \Gamma / \nu$. Results are shown for Cases 1 (red), 2 (blue), 3 (green), and 4 (black).

Figure 15. Time variation of the maximum values of the surface vorticity flux components (a) q_x, (b) q_z, and (c) q_y, and minimum values (d) q_y, normalized with respect to the vortex Reynolds number. Results are shown for Cases 1 (red), 2 (blue), 3 (green), and 4 (black).

Figure 16. (LEFT) Schematic diagram of the model flow field, consisting of a Burgers' vortex sheet (shaded) immersed in a Hiemenz straining flow. (RIGHT) Illustration of vertical vorticity contours during vortex-blade interaction, showing the relationship between the model flow and vorticity dynamics occurring at the blade leading edge during the vortex cutting process.

Figure 17. Variation of (a) dimensionless velocity G and (b) dimensionless vorticity $\partial G / \partial \eta$ as functions of η for a case with $\alpha = 0$. Plots are shown for $\tau = 0$ (A, red), 1 (B, green), 2 (C, blue), 3 (D, orange), and 4 (E, black).

Figure 18. Time variation of dimensionless circulation measures Γ^+ and Γ^- as functions of τ for the example problem shown in Figure 17. For the case with $\alpha = 0$, $\Gamma^+ = \Gamma^-$.

Figure 19. Comparison of profiles of dimensionless velocity $\hat{v}$ as a function of η at $\tau = 8$ (black), 16 (blue), 24 (orange), 32 (red), 40 (green), and 48 (purple). Plots are shown for (a) the vortex cutting simulation described in Section 4 and (b) the simple model described in Section 5.

Figure 20. Time variation of the dimensionless circulation measures Γ^+ and Γ^- as functions of τ for the vortex cutting problem shown in Figure 19. Plots are shown for (a) the vortex cutting simulation described in Section 4 and (b) the simple model described in Section 5.

Table 1. Values of the dimensionless parameters for the reported computations. The blade thickness parameter $T/\sigma_0 = 0.8$ and blade Reynolds number $\mathrm{Re}_B = 1000$ for all cases examined.

Case	Re_V	$\frac{2\pi\sigma_o U}{\Gamma}$
1	3,142	0.5
2	667	2.4
3	157	10
4	79	20

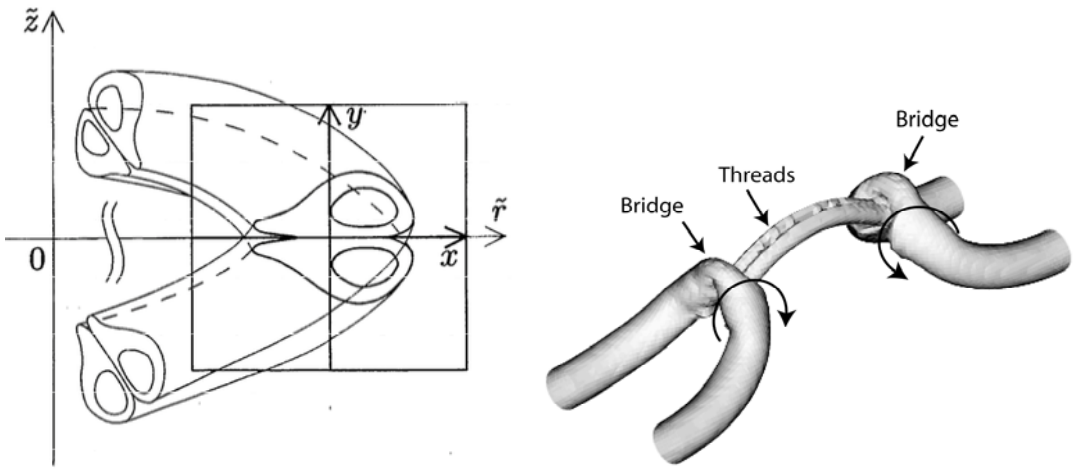

(a) (b)

Figure 1. (a) Deformation of vortex cores into a head-tail configuration (from Kida et al., 1991). (b) Simulation of the reconnection of a vortex pair performed using a triply-periodic spectral method (from Marshall, 2001), showing the direction of the induced velocity from cross-linked regions of the vortex cores and the vorticity threads left over from remnants of the core as the reconnected vortices move apart.

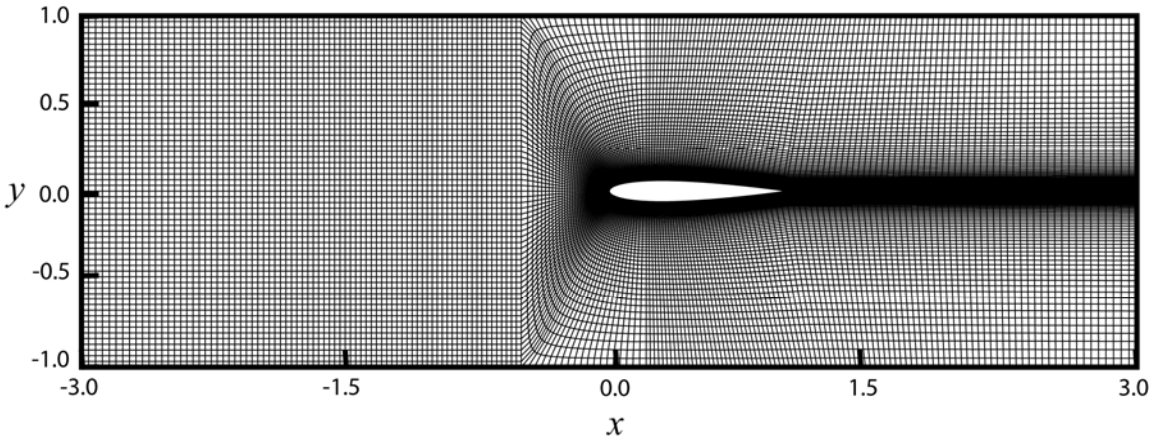

Figure 2. Cross-sectional view of the computational grid in the plane $z = 0$. The inlet and outlet planes are at $x = -3$ and $x = 3$, respectively, and the blade span length is equal to unity.

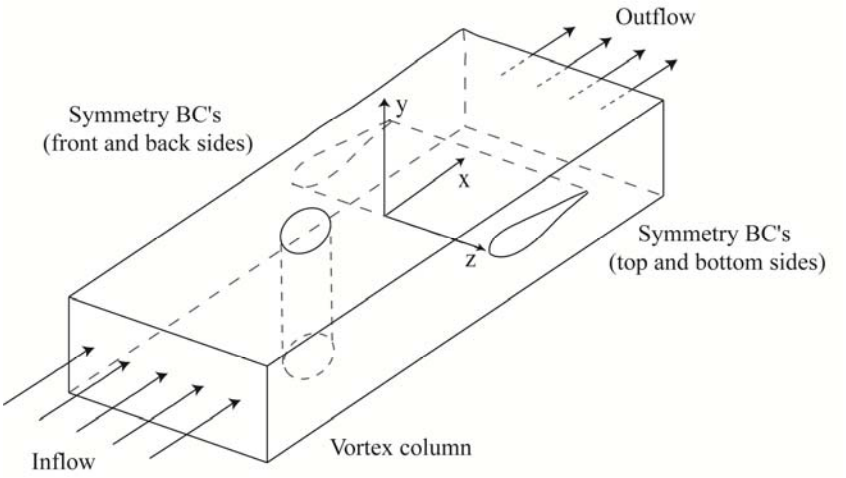

Figure 3. Schematic diagram showing coordinate system and boundary conditions used for the numerical computations.

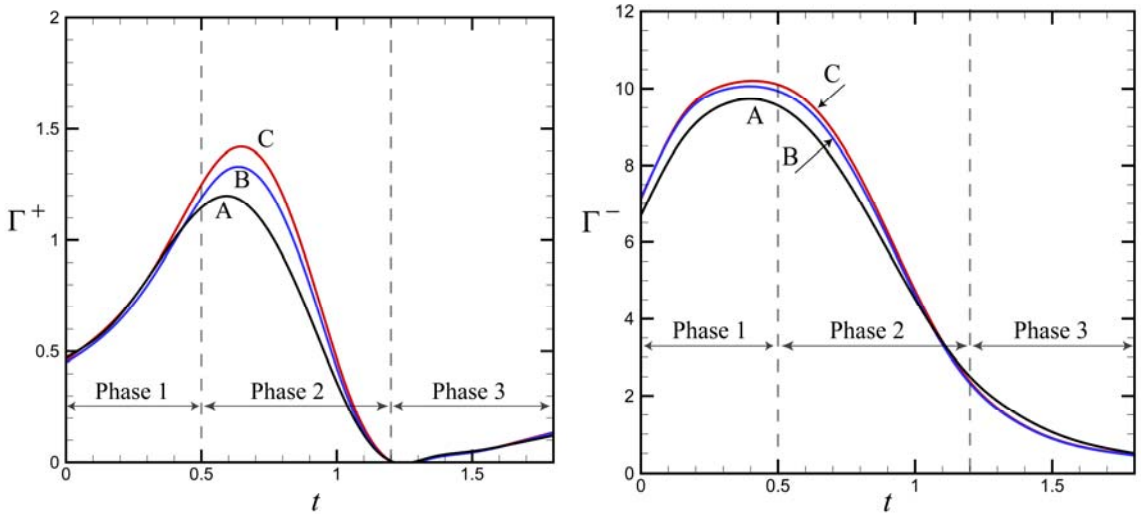

Figure 4. Positive and negative circulation measures, Γ^+ and Γ^-, versus dimensionless time. The circulation was calculated along a line extending out from the blade front in the $-x$ direction over the interval $-1.3 \le x \le 0$ for three different meshes: Mesh A – 865,536 grid points (black), Mesh B – 1,900,701 grid points (blue), and Mesh C – 3,883,238 grid points (red). The three phases of vortex reconnection are identified using dashed vertical lines.

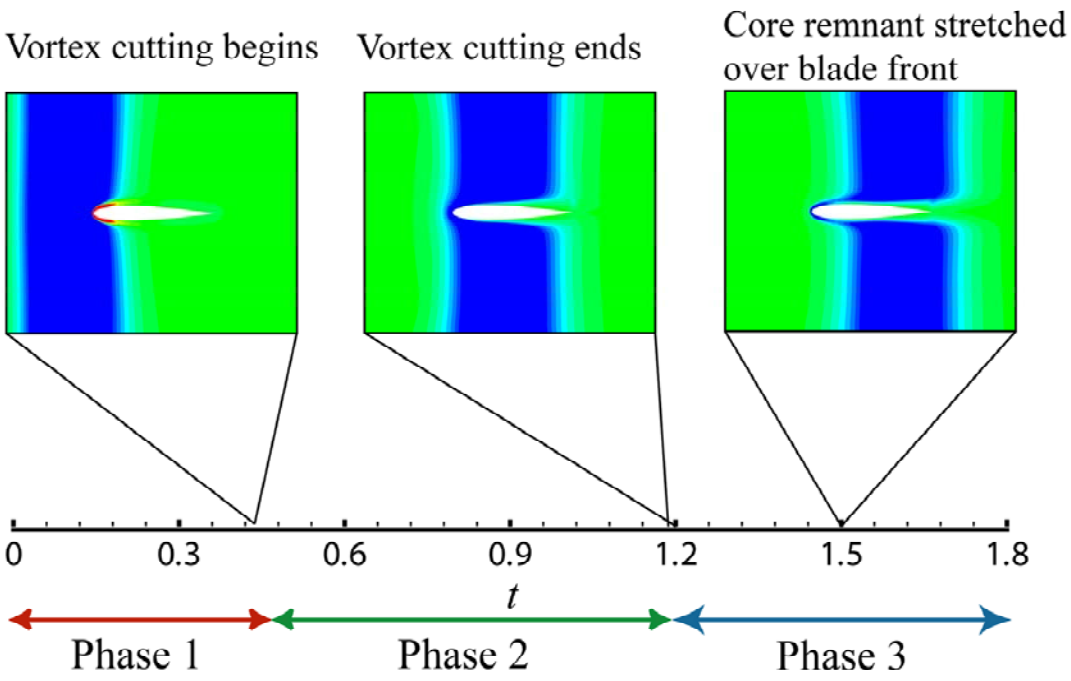

Figure 5. Timeline of the vortex cutting process, showing the three phases of vortex reconnection.

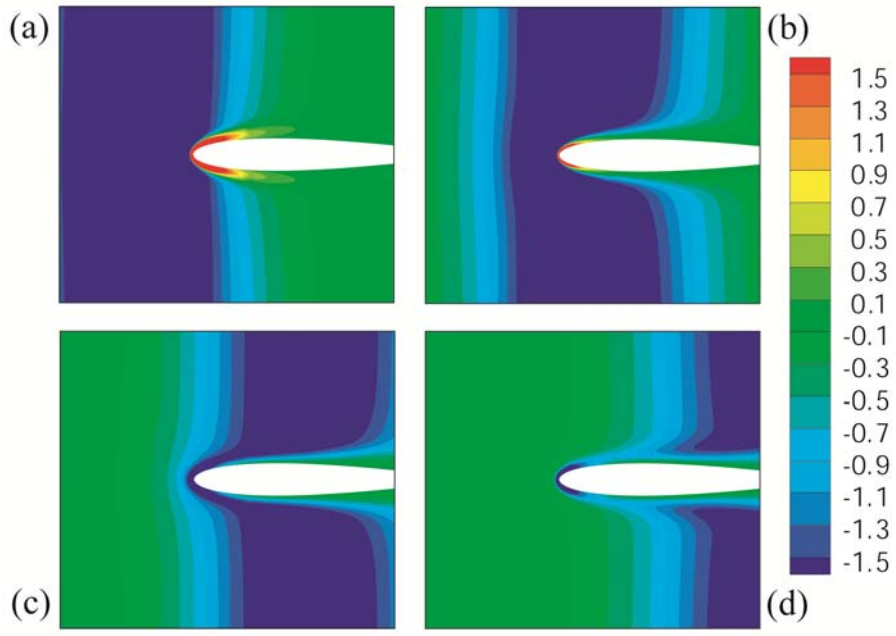

Figure 6. Contour plots from Case 2 showing a close-up of ω_y near the blade from a slice along the blade center span in the *x*-*y* plane for (a) t = 0.75, (b) 1.05, (c) 1.35, and (d) 1.65.

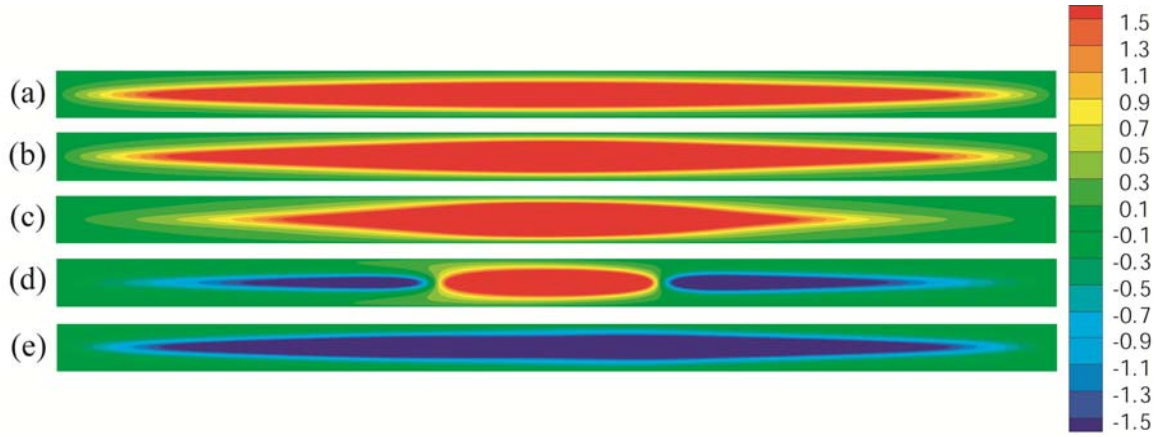

Figure 7. Contour plots from Case 2 of ω_y on the front of the blade for (a) t = 0.15, (b) 0.45, (c) 0.75, (d) 1.05, and (e) 1.35.

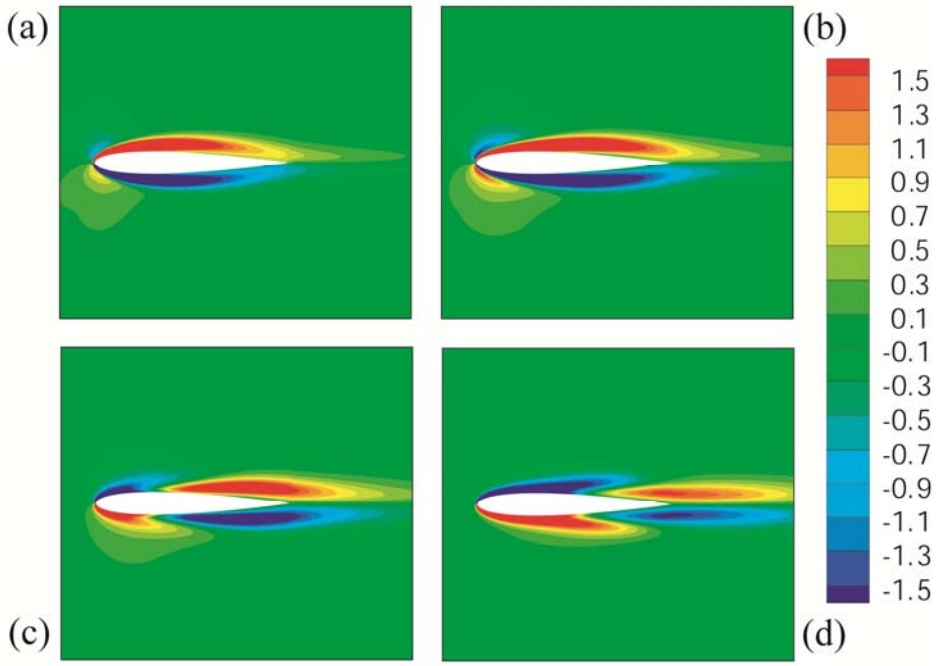

Figure 8. Contour plots from Case 2 of ω_x from a slice along the blade center span in the x-y plane for (a) t = 0.75, (b) 1.05, (c) 1.35, and (d) 1.65.

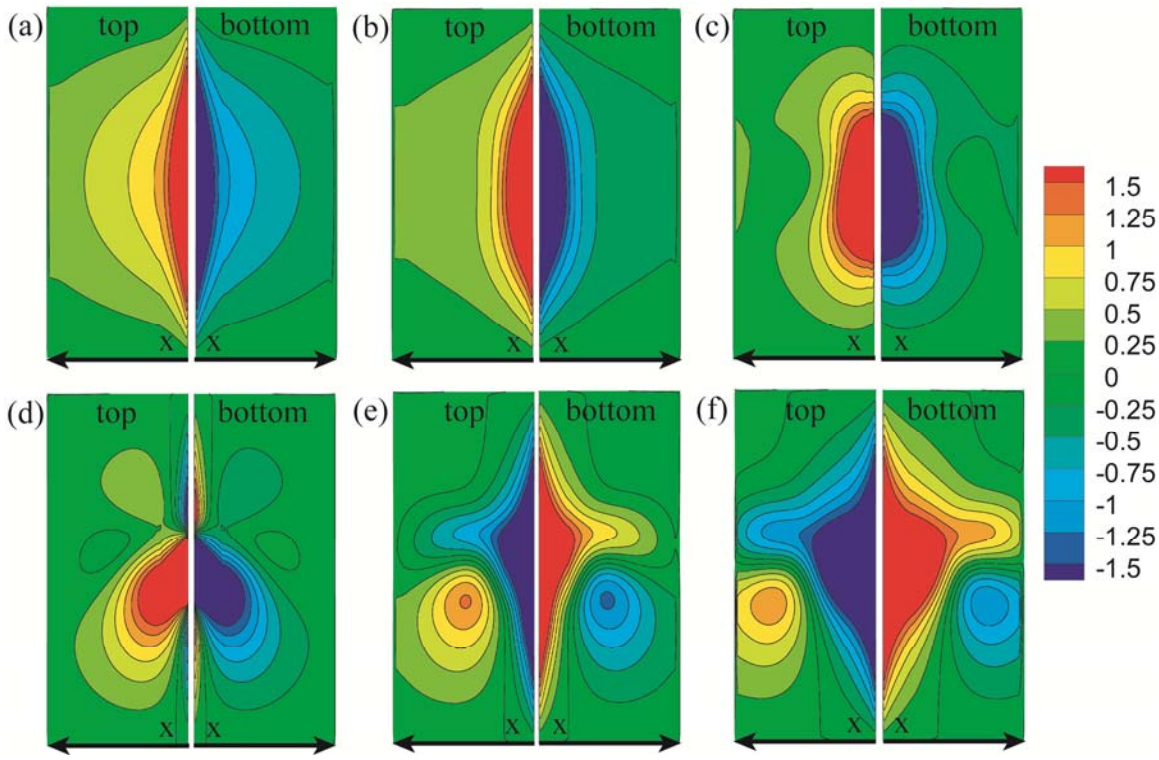

Figure 9. Contour plots from Case 2 of ω_x on the blade top (left) and bottom (right) at (a) t = 0.15, (b) 0.45, (c) 0.75, (d) 1.05, (e) 1.35, and (f) 1.65.

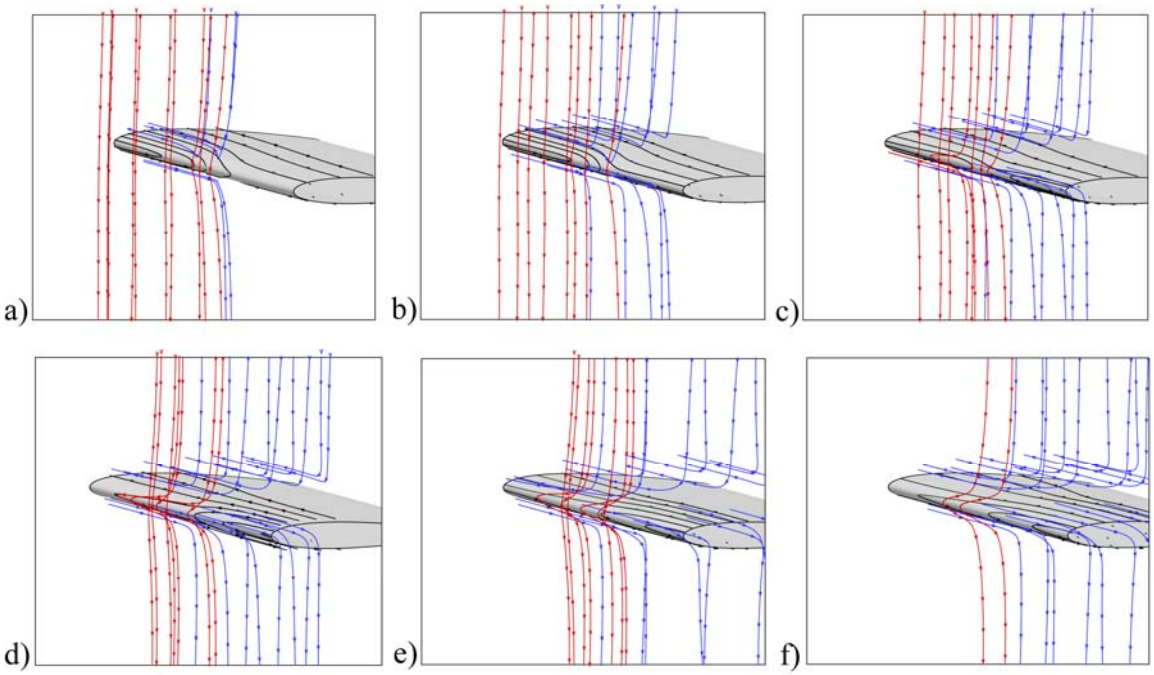

Figure 10. Oblique view of the vortex cutting process. Vortex lines originating in the vortex core can either remain within the vortex core (red) or be cut and reconnect to vortex lines in the boundary layer (blue). Similarly, vortex lines originating within the blade boundary layer can either stay in the boundary layer (black) or join to those originating within the core (blue). Images are shown at times (a) t = 0.75, (b) 0.90, (c) 1.05, (d) 1.20, (e) 1.35 and (f) 1.50. The (uncut) red vortex lines near the blade leading edge become deflected in the spanwise direction as they near the blade.

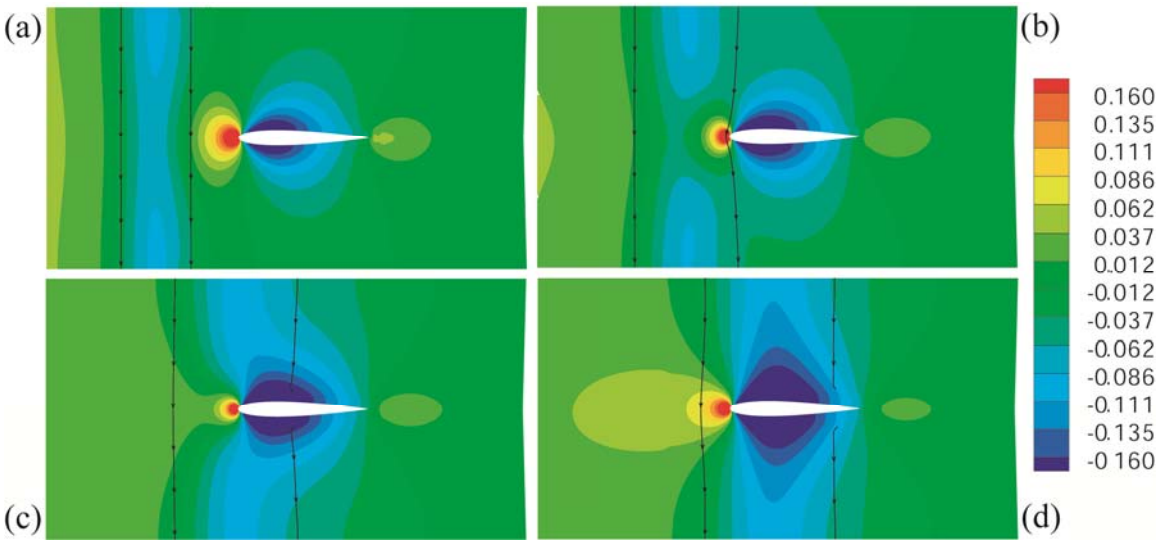

Figure 11. Pressure contours in the *x*-*y* plane passing through the center span of the blade for (a) t = 0.3, (b) 0.6, (c) 0.9, and (d) 1.2. The outlines of the vortex are shown by plotting vortex lines on the two sides of the vortex.

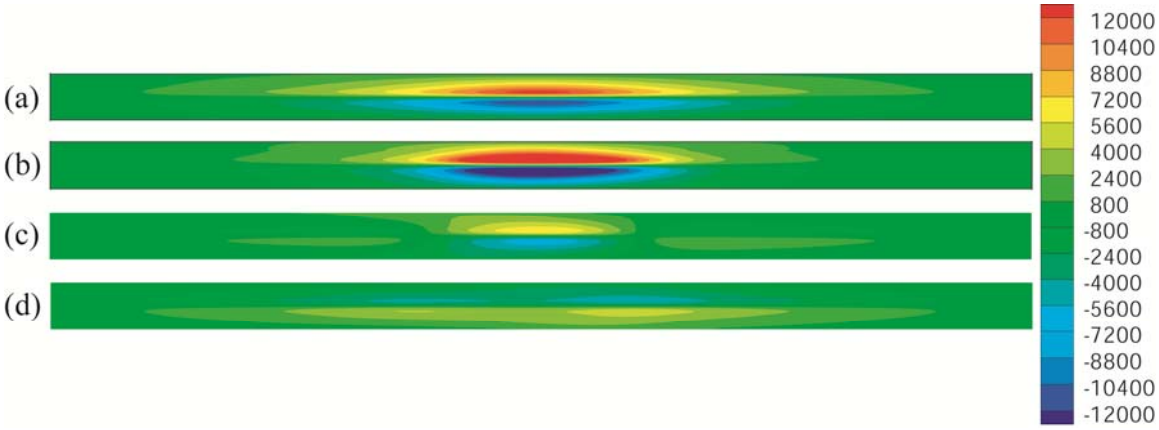

Figure 12. Contour plots of the x component of the vorticity flux, q_x, on blade leading edge, at times (a) t = 0.45, (b) 0.75, (c) 1.05, and (d) 1.35.

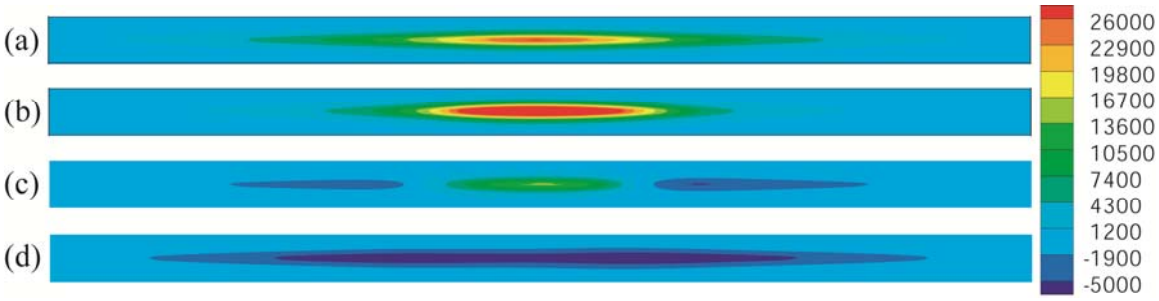

Figure 13. Contour plots of the y component of the vorticity flux, q_y, on the blade leading edge, at times (a) t = 0.45, (b) 0.75, (c) 1.05, and (d) 1.35.

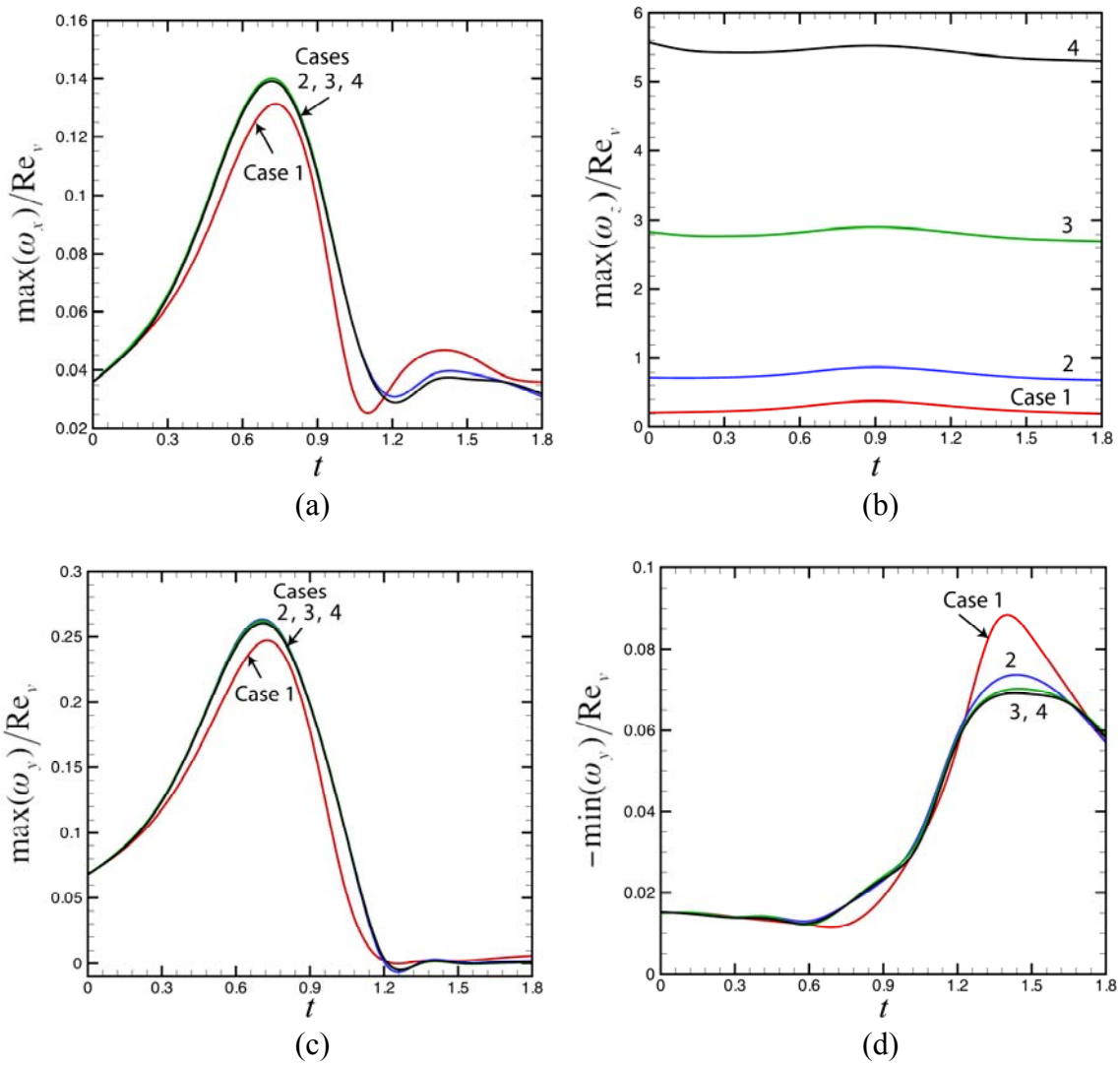

Figure 14. Time variation of (a) maximum ω_x, (b) maximum ω_z, (c) maximum ω_y, and (d) minimum ω_y, normalized with respect to the vortex Reynolds number $\mathrm{Re}_V = \Gamma / \nu$. Results are shown for Cases 1 (red), 2 (blue), 3 (green), and 4 (black).

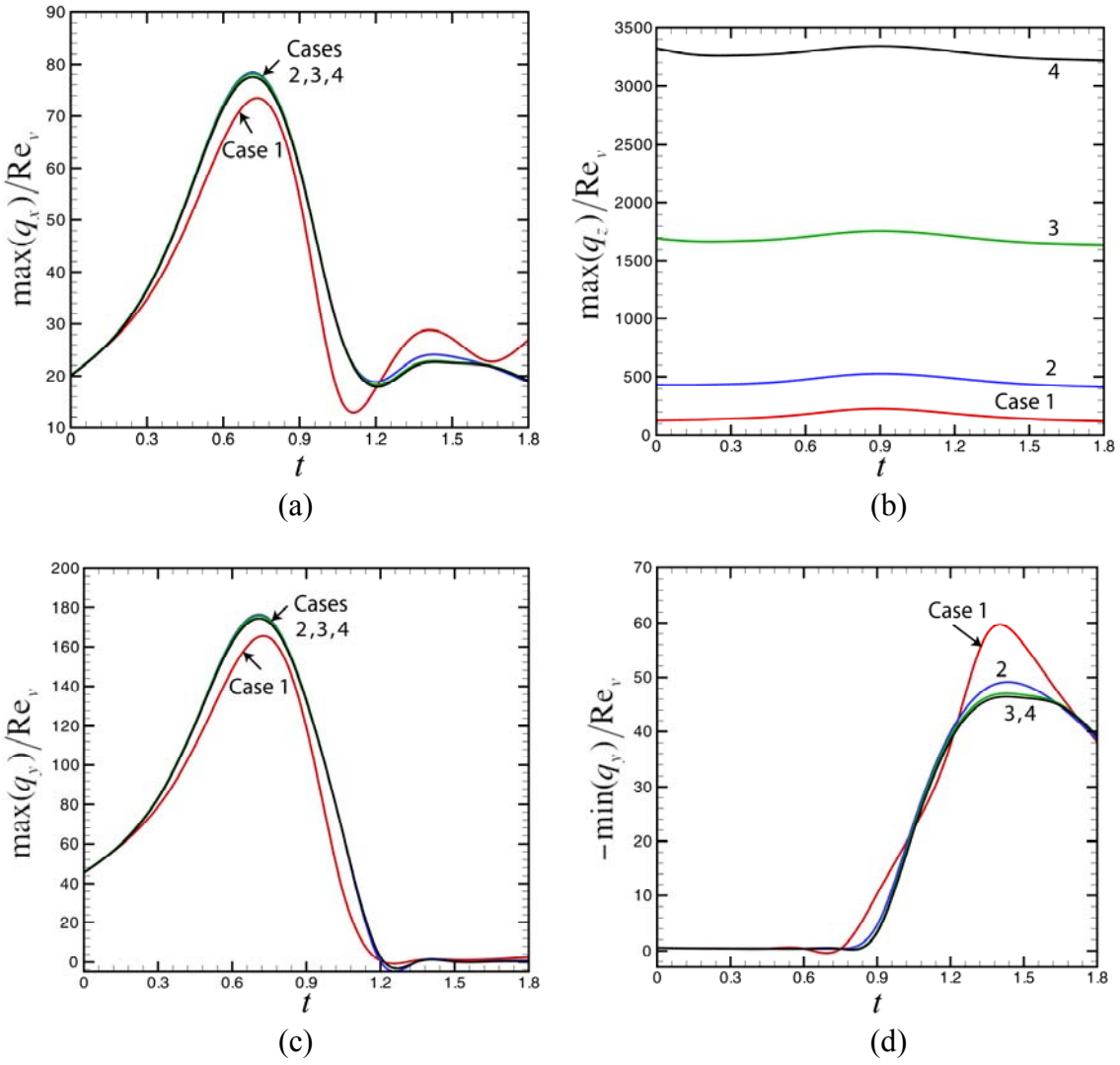

Figure 15. Time variation of the maximum values of the surface vorticity flux components (a) q_x, (b) q_z, and (c) q_y, and minimum values (d) q_y, normalized with respect to the vortex Reynolds number. Results are shown for Cases 1 (red), 2 (blue), 3 (green), and 4 (black).

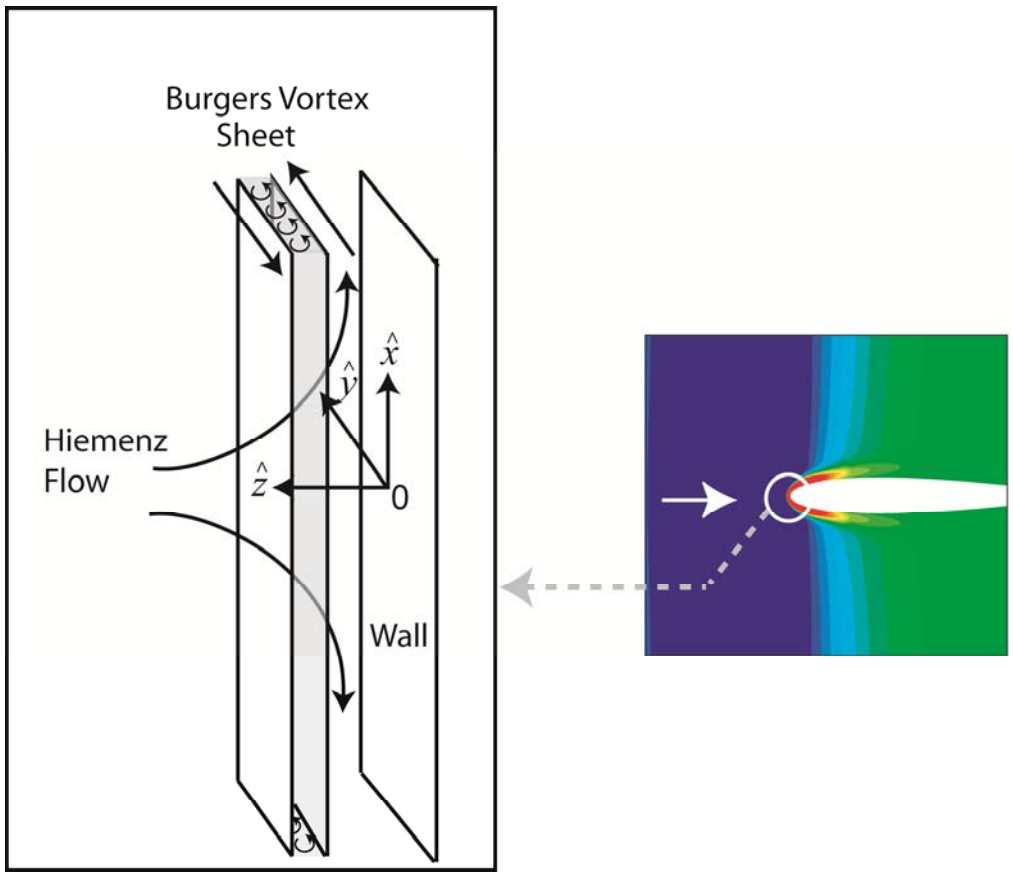

Figure 16. (LEFT) Schematic diagram of the model flow field, consisting of a Burgers' vortex sheet (shaded) immersed in a Hiemenz straining flow. (RIGHT) Illustration of vertical vorticity contours during vortex-blade interaction, showing the relationship between the model flow and vorticity dynamics occurring at the blade leading edge during the vortex cutting process.

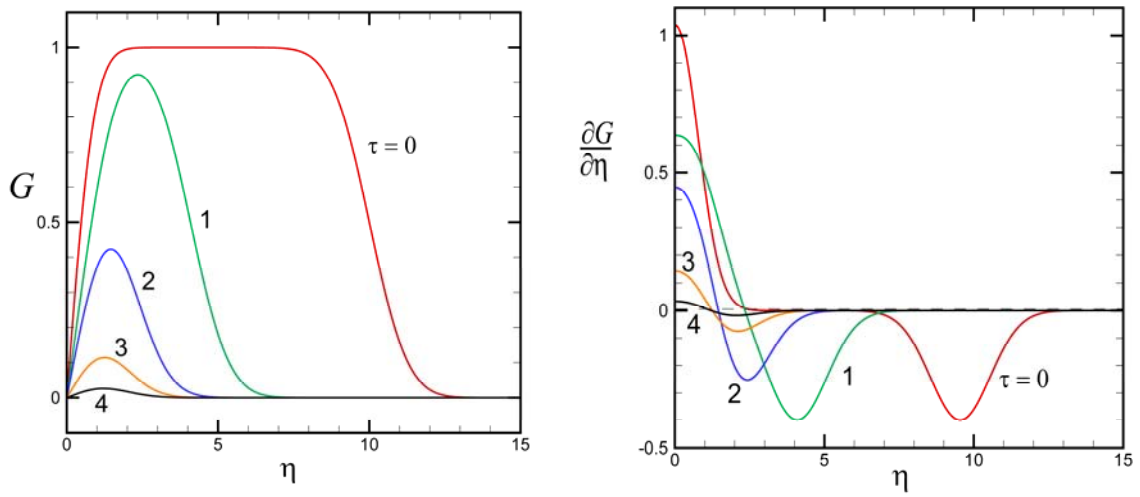

Figure 17. Variation of (a) dimensionless velocity G and (b) dimensionless vorticity $\partial G/\partial \eta$ as functions of η for a case with $\alpha = 0$. Plots are shown for $\tau = 0$ (A, red), 1 (B, green), 2 (C, blue), 3 (D, orange), and 4 (E, black).

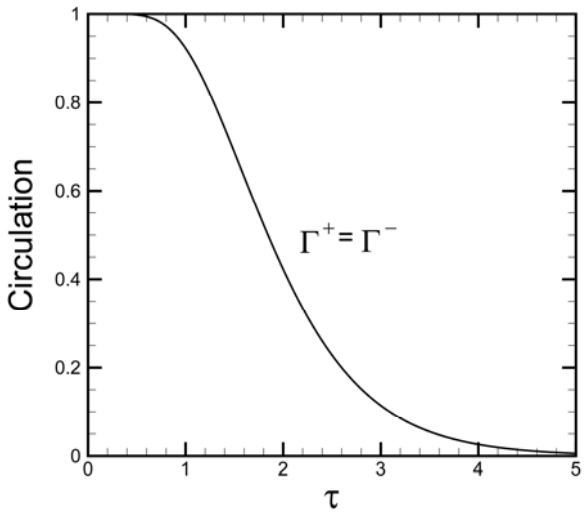

Figure 18. Time variation of dimensionless circulation measures Γ^+ and Γ^- as functions of τ for the example problem shown in Figure 17. For the case with $\alpha = 0$, $\Gamma^+ = \Gamma^-$.

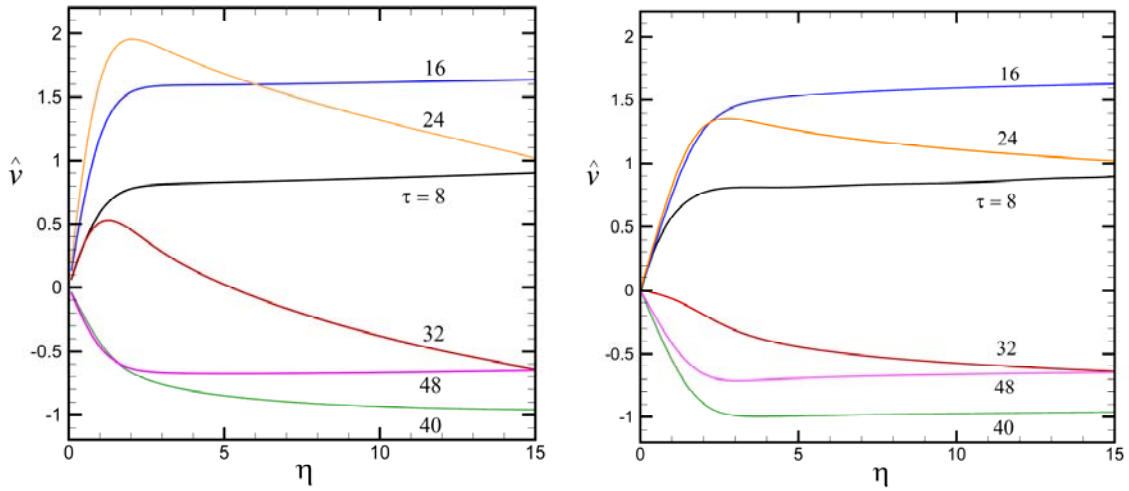

Figure 19. Comparison of profiles of dimensionless velocity $\hat{v}$ as a function of η at $\tau = 8$ (black), 16 (blue), 24 (orange), 32 (red), 40 (green), and 48 (purple). Plots are shown for (a) the vortex cutting simulation described in Section 4 and (b) the simple model described in Section 5.

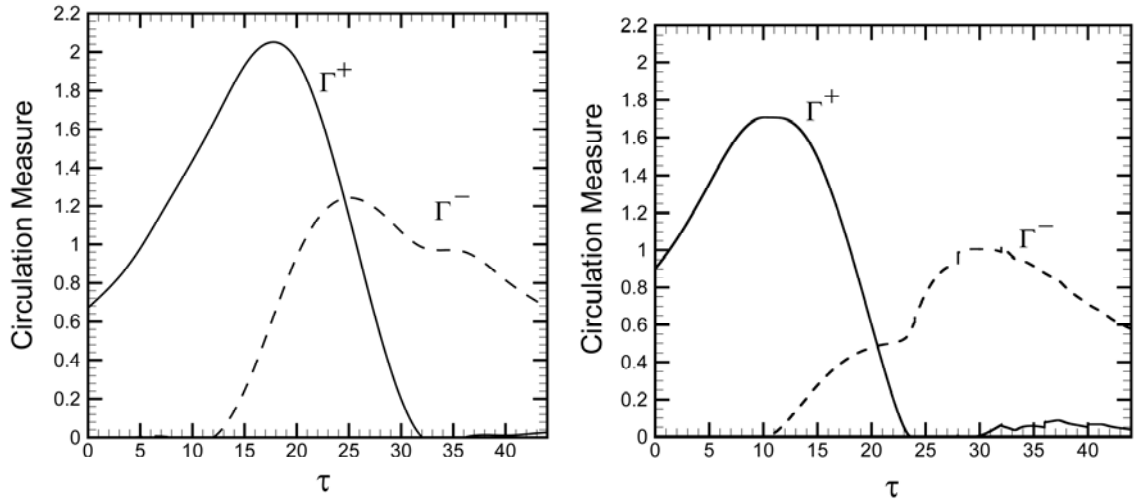

Figure 20. Time variation of the dimensionless circulation measures Γ^+ and Γ^- as functions of τ for the vortex cutting problem shown in Figure 19. Plots are shown for (a) the vortex cutting simulation described in Section 4 and (b) the simple model described in Section 5.